

T. Kathrotia¹, M. Fikri^{2,*}, M. Bozkurt², M. Hartmann², U. Riedel¹, C. Schulz²,
Study of the H+O+M reaction forming OH*: Kinetics of OH*
chemiluminescence in hydrogen combustion systems, Combustion and Flame,
157 (2010) 1261 - 1273

¹Institute of Combustion Technology, German Aerospace Center (DLR) and University of Stuttgart,
Stuttgart, Germany

²IVG, University of Duisburg-Essen, Duisburg, Germany

The original publication is available at www.elsevier.com

<http://dx.doi.org/10.1016/j.combustflame.2010.04.003>

Study of the H+O+M reaction forming OH*:

Kinetics of OH* chemiluminescence in hydrogen combustion systems

T. Kathrotia¹, M. Fikri^{2*}, M. Bozkurt², M. Hartmann², U. Riedel¹, C. Schulz²

¹Institute of Combustion Technology, German Aerospace Center (DLR) and University of Stuttgart,
Stuttgart, Germany

²IVG, University of Duisburg-Essen, Duisburg, Germany

Abstract

The temporal variation of OH* ($A^2\Sigma^+$) chemiluminescence in hydrogen oxidation chemistry has been studied in a shock tube behind reflected shock waves at temperatures of 1400–3300 K and at a pressure of 1 bar. The aim of the present work is to obtain a validated reaction scheme to describe OH* formation in the H₂/O₂ system. Temporal OH* emission profiles and ignition delay times for lean and stoichiometric H₂/O₂ mixtures diluted in 97–98% argon were obtained from the shock-tube experiments. Based on a literature review for the hydrogen combustion system, the key reaction considered was $H + O + M = OH^* + M$ (R1). The temperature dependence of the measured peak OH* emission from the shock-tube and the peak OH* concentration from a homogeneous closed reactor model are compared. Based on these results a reaction rate coefficient of $k_1 = (1.5 \pm 0.4) \times 10^{13} \exp(-25 \text{ kJmol}^{-1}/RT) \text{ cm}^6 \text{ mol}^{-2} \text{ s}^{-1}$ was found for the forward reaction (R1) which is slightly higher than the rate coefficient suggested by Hidaka et al. (1982). The comparison of measured and simulated absolute concentrations shows good agreement. Additionally, a one-dimensional laminar premixed low-pressure flame calculation was performed for where absolute OH* concentration measurements have been reported by Smith et al. (2005). The absolute peak OH* concentration is fairly well reproduced if the above mentioned

* Corresponding author: mustapha.fikri@uni-due.de

rate coefficient is used in the simulation.

Introduction

In H_2/O_2 combustion, emission of UV radiation at a wavelength of around 306 nm is observed due to the transition of the hydroxyl radical from its electronically excited state ($A^2\Sigma^+$) to its ground state ($X^2\Pi$). While the OH^* emission is weak in reacting H_2/O_2 mixtures it is strong in hydrocarbon flames [1]. OH^* is much less (more than five orders of magnitude) abundant than some of the important ground state intermediate species (OH , H , O) and thus has nearly no influence on the overall hydrogen oxidation. However, due to its spontaneous emission of light, studies of this excited radical have gained importance because it has been used as an optical marker in combustion diagnostics over years. Chemiluminescence has the potential to provide information from the flame by using inexpensive optical detection equipment.

The kinetics of OH^* involve its formation from energy-rich intermediates and its consumption by collisional quenching and dissociation. Deactivation by radiative decay is typically negligible for the description of the OH^* concentration but is responsible for the chemiluminescence signal. Several routes have been suggested for the formation of OH^* among which $\text{H} + \text{O} + \text{M} = \text{OH}^* + \text{M}$ (R1) is considered to be the major contributor along with some contribution of $\text{H} + \text{OH} + \text{OH} = \text{OH}^* + \text{H}_2\text{O}$ (R6). Several studies of the formation pathway of OH^* from these reactions have been carried out in the past. Scattered work has been published so far on flame and shock-tube measurements with the objective to determine the rate coefficient of these reactions. Early studies of OH^* lead back to 1959 when Kaskan [2] studied OH^* emission in rich $\text{H}_2/\text{O}_2/\text{N}_2$ flames. Later, shock-tube studies were reported by Hidaka et al. [3] and Koike et al. [4]. Among recent studies, Hall et al. [5] performed shock-tube experiments and determined the rate coefficient of the reaction (R1). Smith et al. [1] recommended values for the rate coefficient of reaction (R1) and (R6) based on experiments in one-dimensional premixed H_2/air flames. To our knowledge, this is the only available measurement of absolute OH^* concentrations in hydrogen/air flames. Recently, the formation mechanism of OH^* was studied by an *ab-initio* analysis by Skrebkov et al. and Smekhov

et al. [6-8].

The aim of the present work is to study the kinetics of the major OH* forming reaction $H + O + M = OH^* + M$ (R1) in a wide range of conditions and to describe its kinetics in order to reproduce temporal intensity profiles measured during the ignition process. Furthermore, the reaction mechanism obtained was compared against absolute species concentrations in laminar flames.

This paper is divided into five sections. The first section provides a brief review on OH* kinetics. The second section discusses the shock-tube experiments. It is followed by the description of the chemical kinetics model in the third section. An analysis of the temperature dependence of the rate coefficient k_1 of reaction (R1) is discussed in the fourth section. In the last part, results of the ignition delay times from the shock-tube studies are compared to simulation results and different reaction sensitivities with respect to OH* formation are discussed. A calculation for a rich, laminar, one-dimensional, premixed burner-stabilized flame based on our kinetics data is compared to respective data from literature.

OH* kinetics

OH* formation and depletion can be modeled by a set of elementary reactions, given by the following reaction scheme:



Reaction (R1) is a three-body recombination reaction important at low temperatures (below 2800 K). Its reverse reaction (R-1) acts as a dominant OH* consumption path at temperatures above 2800 K [3-4]. OH* is unstable and returns to the ground state by either emitting light ($h\nu$) by

reaction (R2) or by collisional energy transfer (R3).

Studies revealed that OH* is mainly formed by reaction (R1) in the combustion zone where H atoms combine with atomic oxygen involving a third collision partner in a recombination reaction. This reaction is exothermic with $\Delta_f H^{298} = -36.99 \text{ kJmol}^{-1}$, where information on the heat of formation at 298 K for OH*, H and O species is given in the Burcat and McBride database [9]. The formation of OH* at temperatures below 2800 K is mainly due to reaction (R1) whereas the reverse reaction (R-3) (OH* formation by thermal excitation) becomes more dominant at temperatures above 2800 K.

An early study of OH* emission is published by Kaskan in 1959 [2] who investigated 'abnormal' excitation of OH in H₂/air flames. They found that the OH* emission intensity was proportional to the cube of the ground state OH concentration and suggested a set of possible radical recombination reactions responsible for the formation of OH*. They proposed $\text{H} + \text{O} = \text{OH}^*$ as well as $\text{H} + \text{OH} + \text{OH} = \text{OH}^* + \text{H}_2\text{O}$ as the most likely reactions. Gutman et al. [10] concluded from studies in reacting H₂/O₂ mixtures that the reaction (R1) is the main source of OH* but were unable to determine the role of the third body. Later, Koike et al. [4] provided the rate coefficient of reaction (R1) by correlating the emission intensity at various temperatures and calculated OH* concentrations. Similarly, Hidaka and co-workers [3] identified reaction (R1) as the main source of OH* from shock-tube experiments with diluted H₂/O₂/Ar mixtures and derived a reaction rate coefficient of $1.2 \times 10^{13} \exp(-29 \text{ kJ}/RT) \text{ cm}^6 \text{ mol}^{-2} \text{ s}^{-1}$. Among recent studies, Smith et al. [1] examined rich hydrogen/air premixed flames. Based on modeling and experimentally obtained OH* number densities, they recommended the rate coefficient of the reaction (R1) to be $5.45 \times 10^{12} \text{ cm}^6 \text{ mol}^{-2} \text{ s}^{-1}$. The shock-tube study performed by Hall et al. (2006) [5] derived the rate coefficient of reaction (R1) by fitting the temperature dependence of the OH* peak intensity in H₂/O₂ mixtures. In all these studies, the recommended rate coefficient varies by two orders of magnitude from each other. Arrhenius plots with the rate coefficients discussed above are shown in Figure 8 (presented later in the paper). A few authors have recently suggested the formation of OH* from the reaction



which was used by Marques et al. [11] in their acetylene combustion model and the reaction



suggested by Skrebkov et al. [6] to also contribute to OH* formation. In [11] the rate coefficient of reaction (R4) in C₂H₂/O₂ system is assumed to be identical to the rate coefficient of the ground state reaction H + O₂ = OH + O. They found through a production rate mechanism that reaction (R4) as a principle path then would contribute to about 90% of the total OH* formation. They stated that by removing the reaction (R4) from their proposed mechanism, no agreement was found between simulated and measured chemiluminescence profiles. In the current work it was seen that an incorporation of this reaction in the kinetics model significantly alters not only the ground state chemistry but also the chemiluminescence profiles. Therefore, (R4) was not incorporated in our OH* sub-mechanism.

The OH* formed is short lived and returns to the ground state via two channels. In the first channel, it emits its excess energy in form of light in a radiative decay (R2). The rate coefficient of this reaction has been proposed by several authors [3, 12-13]. The second channel is the non-reactive collisional quenching reaction (R3). Here, the excess energy of OH* is transferred to the collision partner M. The effect of O₂, H₂, H₂O, N₂, H, OH, and Ar have been studied at various temperatures ranging from room temperature to flame temperature by several authors [14-19]. Becker et al. [17] provided quenching rate coefficients for M = H₂, H, Ar at room temperature. Fluorescence excitation by a dye laser was applied to measure the OH* lifetime in presence of H₂, H, Ar. Fairchild et al. [14] measured thermally-averaged collisional quenching with H₂O, O₂, H₂ by laser-induced fluorescence (LIF) at about 1100 K. The OH* quenching with H₂O and atomic H was studied by Jeffries et al. [20] in low-pressure stoichiometric H₂/O₂/N₂O flames also using LIF. A recent study of Bailey et al. [16] investigated the temperature dependence of OH* quenching for collision partners such as N₂, O₂ at room temperature. Hemming et al. [15, 19] studied the influence of N₂, O₂ and H₂ at and below room temperature. Heard et al. [18] determined the H₂

quenching rate coefficient at low temperatures (200–344 K) in a flash-photolysis system. All these quenching rate coefficients data are in good agreement with each other from room to flame temperature. For collision partners such as H, O, and OH limited information is available only due to the complexity of the measurement. The compilation of data for major collision partners is given by Tamura et al. [21] and recommendations are made for the 300–2500 K range. Figure 1 provides information on the major OH* quenching rate coefficients in an Arrhenius plot. The ratio of the rate coefficients of (R2) and (R3) determines the quantum yield of the chemiluminescence. With $k_3 > k_{-1}$ and $k_3[M] > k_2$ under our present experimental conditions, OH* is mainly depleted by reaction (R3).

Experimental

The OH*-chemiluminescence signals of reacting stoichiometric and lean, highly diluted H₂/O₂ mixtures have been investigated in a shock tube with a constant inner diameter of 79 mm. The driver section is 3.5 m long and is pumped down to 10⁻² mbar. The driven section with a length of 5.7 m is pumped down to 10⁻⁸ mbar using a turbomolecular pump before preparing a new filling. The two parts of the shock tube are separated by a 50 μm aluminum diaphragm. A schematic setup of the shock tube is shown in Figure 2.

Mixtures are prepared in a stainless steel vessel using the partial pressure method. Stated chemical purities were 99.998% for O₂, 99.999% for H₂, 99.999% for N₂ and 99.9999% for Ar. The incident shock velocity was determined using four piezoelectric pressure transducers placed near the endflange. The temperature T_5 and pressure p_5 behind the reflected shock wave were computed from the measured incident shock velocity using a one-dimensional shock-tube model (shock-tube code of the CHEMKIN package [22]) with respect to the initial conditions p_1, T_1 .

Optical ports are located 40 mm upstream of the endflange and allow the detection of the chemiluminescence signal. Measuring chemiluminescence with high temporal resolution requires to limit the detection to a small area within the shock tube. A slit was placed at some distance in

front of the detector to limit the detection solid angle. A width of 1 mm was selected to provide an optimal balance between signal strength and time resolution. This setup provides a time resolution of $\sim 1 \mu\text{s}$ as determined from the light collection angle and the passing velocity of the reflected shock wave. An interference filter at 307 nm (10 nm full width at half maximum) limits the detection to OH^* chemiluminescence from the diagonal transitions in the A-X system. The OH^* signal is amplified by a photomultiplier (Hamamatsu 1P28) with a constant amplification voltage for all presented measurements. In order to ensure sufficient time resolution of the signal detection, a $10 \text{ k}\Omega$ resistor was connected in parallel to the amplifier of the PMT raw output. The time resolution of the setup was investigated for different resistors by investigating the pulse detected from the input of a short square signal pulse of a LED. A balance between time resolution and signal intensity was considered. The time resolution of the chosen detector is $1 \mu\text{s}$ and thus matches the resolution of the optical arrangement. Linear response of the PMT was also respected by the choice of the resistance. Care has been taken to not disturb the optical configuration during all set of the experiments to allow for a direct comparison of signal intensities.

Figure 3 shows the pressure profile and emission intensity for two experiments with 1% O_2 + 1% H_2 in Ar at $p_5 = 1.2 \text{ bar}$ and $T_5 = 1674 \text{ K}$ (upper curve) and 1% O_2 + 2% H_2 in Ar at $p_5 = 1.15 \text{ bar}$ and $T_5 = 1622 \text{ K}$ (lower curve). The pressure trace shows a two-step increase due to the incident and the reflected shock wave. The appearance of the reflected shock wave defines t_0 . At $t = 88 \mu\text{s}$ (for the lean mixture) the onset of the emission signal can be detected, defining the ignition delay time τ . The experimental conditions of all experiments are summarized in Table 1.

The pressures and temperatures behind the incident and the reflected shock waves are determined from the velocity of the incident wave. Non-ideal effects behind the reflected shock wave cause an uncertainty of the temperature T_5 behind the reflected shock wave of 5–15 K. The pressure trace show a minor decay in pressure during the test time of 1–2 ms which is attributed to temperature effects on the pressure transducers. Coating the pressure transducers with high-temperature silicone (RTV) almost eliminated this effect. Therefore, we are confident that the 1-D

assumption for the determination of T_5 is valid. At high temperatures ($T > 3000$ K) some of the OH* signal traces showed significantly increased signal with a peak in the OH* signal early after ignition. As stated in [23] this could be a result of ignition events that lead to detonations and hence to an acceleration of the reaction. In this study the experiments that showed perturbed OH* intensity profiles were discarded. The measurements at low temperatures are immune against this effect and are highly reproducible.

Chemical kinetics model

The kinetics model for OH* chemiluminescence includes reactions forming and consuming OH* as described in the previous section and a complete hydrogen oxidation mechanism. The entire mechanism considered in the present work is summarized in Table 2. The basic mechanism of hydrogen oxidation which consists of 10 species and 46 reactions is adopted from the Warnatz mechanism [24]. It includes temperature- as well as pressure-dependent reactions and has recently been documented [25]. The rate coefficients of the elementary reactions are based on the recommendations of Baulch et al. [26]. This mechanism is validated with respect to flame velocity (5–70 fuel percentage) and ignition delay times in the temperature range from 950–3000 K. The absolute concentration of the major species (H_2 , O_2 , H_2O , H , OH , O) is in very good agreement with species concentration measurements from [27] as presented in the results section. Additional mechanism validations are presented in Appendix A.

The OH* sub-mechanism with the reactions discussed above is added to the base mechanism. A new rate coefficient of the key reaction (R1) is suggested in the present work. The rate coefficient of the radiative decay reaction (R2) chosen in the present work is $k_2 = 1.45 \times 10^6 \text{ cm}^3 \text{ mol}^{-1} \text{ s}^{-1}$ as given in [28]. The value for k_2 chosen here deviates by 30% from the lowest and 17% from the highest literature value. The quenching rate coefficients k_3 are taken from the recommendations of Tamura et al. [21] except for $M = \text{Ar}$ which is from Paul et al. [12]. The thermodynamic data of OH*, used for calculating the rate coefficients of the reverse reaction is from the Burcat and McBride

database [9] whereas for all other species we use data derived from computed fits based on the values reported in the JANAF tables [29]. The results from the shock-tube measurements were also compared to the widely accepted GRI-mech 3.0 as a base hydrogen mechanism. The hydrogen oxidation mechanism of the present work and GRI-mech 3.0 are validated at a wide range of conditions [26, 30]. Both mechanisms differ in the selection of the rate coefficient for reaction (R8) as well as in the rate coefficients for HO₂ and H₂O₂ formation. In GRI-mech 3.0, k_8 is closer to the rate coefficient from [30] whereas in the present work we use the value recommended recently in [26]. Although this newer rate coefficient is stated to be an improved fit to lower temperature data, the rate coefficient from [30] is widely accepted. This rate coefficient k_8 has nearly no influence on the OH* temperature dependence presented later. Another difference in both mechanisms is the higher values of HO₂ and H₂O₂ formation rate coefficients (k_{14} , k_{21}) in our mechanism. With this selected rate coefficient the ignition delay time measurements near 1000 K very well predict the shock-tube experiments reported in [31] and support our selection of rate coefficients for HO₂ and H₂O₂ formation.

The mechanism for OH* chemiluminescence is compared to absolute OH* concentration measurements from shock-tube experiments (present work) and absolute concentration measurements from premixed laminar flames by Smith et al. [1]. Species concentration profiles are calculated with the Fortran code HOMREA [32] based on a zero-dimensional (0-D) homogeneous closed reactor model with the initial mixture composition and the initial temperature and pressure behind the reflected shock wave as input. Constant volume is assumed and the temperature is calculated for adiabatic conditions. Additionally, absolute concentrations in burner-stabilized premixed laminar flames are simulated with 1-D flame code INSFLA [32-33] in order to get insight into the predictions of the kinetics model. Initial mixture composition, gas flow rate, temperature and pressure at the burner surface are used as input. This model also requires the measured temperature profile as an input to account for heat losses. In order to provide good spatial resolution in the flame zone, 81 grid points are used together with grid adaptation techniques in the flame calculations.

The hydrogen oxidation mechanism including the chemiluminescence sub-mechanism used in this work contains 11 reacting species and 64 elementary (forward and backward) reactions. In the initial computation we used the rate coefficient of reaction (R1) from literature that was then improved in this work according to the strategy described in the next section. The ignition delay time and the flame data presented in the results section are based on calculations considering the recommended reaction rate coefficient of reaction (R1) from this work.

Calibration of measured OH* chemiluminescence intensities

The OH* emission intensity measured under shock-tube conditions cannot be directly related to the computed concentrations because information about the relationship between the recorded intensity and the absolute concentration of the excited species requires calibration. It is known from previous studies [3-4] that above 2800 K the OH* concentration is determined by the thermal excitation reaction (R-3) and is independent from the rate coefficient of reaction (R1). This allows to calibrate the measured peak emission intensity, and thus OH* concentration, with simulated peak concentrations at such temperatures. The resulting calibration constant can then be used to quantitatively link the measurement and the simulation for all experimental conditions and therefore allows to interpret the temperature dependence of reaction (R1). The systematic errors originating from the intensity measurements that are used for the calibration measurements are in the $\pm 20\%$ ($1-\sigma$) range. For the calibration constant we used the average value of twenty measurements.

There are three important points that must be clarified before relying on this strategy: (i) Additional reactions (for example collisional induced decomposition of OH*) must have a negligible effect, (ii) it must be clarified that the measured peak intensity does not suffer from insufficient temporal resolution of the detectors (thus, reduced sensitivity due to the convolution with the signal transfer function) and (iii) the influence of radiation trapping due to ground state OH must be negligible or quantifiable.

(i) Although the dissociation according to reaction (R-1) is thermodynamically accessible (37.6 kJ mol^{-1}), the rate is slow compared to the thermal excitation reactions that form OH^* through (R3) at high temperature. In order to see the effect of dissociation of OH^* via reaction (R-1) at high temperatures, a sensitivity analysis was performed. For mixture A at 3000 K and 1 bar, Figure 4 shows the sensitivity analysis with respect to OH^* for the variation of the reaction rate coefficients of the different relevant reactions. At this temperature, thermal excitation dominates the OH^* formation, the maximum sensitivity in respect to OH^* concentration is with (R-3) and collision partners $M = \text{H}_2\text{O}, \text{Ar}, \text{O}_2, \text{H}_2$. The reactions (R1) and (R-1) show some sensitivity, however, the overall effect of both reactions is much lower than that of the thermal excitation (R-3). A reaction flow analysis for this condition shows that the relative contribution to variations in the OH^* peak concentration is to 95% due to reaction (R-3) (with the contributions of $M = \text{H}_2\text{O}$ (37%) + OH (23%) + Ar (16%) + O_2 (10%) + H_2 (5%) + H (4%) for the given bath gas). In comparison, the reverse of the chemical excitation reaction (R-1) contributes 5% to the OH^* peak concentration only. Therefore, we can neglect the contribution of reaction (R-1) at our calibration conditions.

(ii) The time resolution of the experiment that is determined by the observed solid angle and the electronic properties of the PMT/amplifier system is $1 \mu\text{s}$ which is short enough to not influence the signal traces.

(iii) Signal emitted from OH^* chemiluminescence detected at $\sim 307 \text{ nm}$ is partially trapped by ground state OH which is abundant in the gases after ignition. We used a simple analytical approach to quantify signal trapping for our experimental conditions that accounts for the homogeneous luminous and homogeneously absorbing gas mixture within the shock tube (79 mm maximum path length) for all the mixtures used in this study. To quantify signal trapping two OH lines $R_1(7)$ and $R_1(11)$ for the R-branch bandhead of the OH A-X (0,0) band were investigated. For both lines the peak maximum leads to a reduction in the detected OH^* signal by $\sim 10\%$. For all measured conditions the calculated attenuation was almost constant. For the calibration condition, the higher [OH] concentration that is related to the higher temperature is compensated by lower absorption cross sections, also resulting in an overall $\sim 10\%$ signal trapping at the peak

maxima. Therefore, the signal trapping effect is covered by the calibration. The error of the calibration caused by signal trapping due to slight variations between calibration and measurement and due to variations in the time profile is estimated to be in the $\pm 3\%$ range.

Taking this into account and by knowing that the OH* chemiluminescence formation is overwhelmed by reaction (R-3) for $T > 2800$, a calibration factor was obtained by relating the peak OH* intensity measured to the peak OH* concentration at data points above 3000 K. The calibration procedure is performed at all four mixture conditions with 19 data points and an average value was taken. A calibration factor of $2.62 \times 10^{-18} \text{ cm}^3 \text{ mol}^{-1} \text{ mV}^{-1}$ was deduced.

The calibration was then adopted to describe the measured chemiluminescence intensities throughout the full temperature range of our experiments. This allows to quantitatively compare measured intensities attributed to the formation paths (R1) and (R3) at temperatures lower than 2800 K and calculated concentrations throughout the temperature range of interest and, thus, to investigate the temperature-dependent OH* concentration from the signal intensities.

Result and Discussion

Determination of the T-dependent maximum OH concentration*

A typical temporal variation of the OH* concentration in hydrogen combustion consists of an initial rapid formation of OH* from reaction (R1) followed by slow depletion mainly due to the radiative decay (R2) and collisional quenching by reaction (R3). Figure 5 shows the temporal variation in OH* concentration for a lean H₂/O₂/Ar mixture A at 1592 K initial temperature (T_5) and 1.27 bar pressure behind the reflected shock wave (p_5). The shape of the profile and the position time on time axis is well reproduced when compared to the experiment. The measured absolute concentrations based on the calibration method described before are in good agreement with the simulations.

The mixture compositions studied in the shock-tube experiments are listed in Table 1. Figure 6 shows the temperature dependence of the OH* signal and simulations for mixtures A, B, C and D. Here, the measured peak intensities ($I_{\text{OH}^*,\text{max}}$) are converted to the respective concentrations using the calibration factor discussed in the earlier section. In the figure the shock-tube data for mixture A, B, C and D are shown as closed symbols whereas the respective simulated peak concentrations $[\text{OH}^*]_{\text{peak}}$ are shown as open symbols connected by lines. The rise in OH* concentration in the induction phase is determined by ground state chemistry as shown in Figure 7. It presents the normalized local sensitivity coefficients over the reaction time for $\phi = 0.5$, $T_5 = 1900$ K, $p_5 = 1$ bar. During the rise in OH* the reaction $\text{H} + \text{O}_2 = \text{OH} + \text{O}$ has the maximum sensitivity. However, when the OH* concentration reaches its maximum, the most influential reaction is (R1). The reaction $\text{H} + \text{OH} + \text{OH} = \text{OH}^* + \text{H}_2\text{O}$ (R6) has a 10 times reduced sensitivity compared to (R1). In addition, the maximum sensitivity of the quenching reactions ($\text{M} = \text{H}_2\text{O}$) at the OH* peak is 26% only. Thus, the concentration of OH* at the peak is mostly determined by the rate coefficient of reaction (R1). Therefore, the peak height was used to obtain the rate coefficient of the reaction (k_1) by accounting for the quenching reactions using kinetics data from the literature.

The OH* concentrations predicted from different k_1 values were compared to the measured converted concentrations at different temperatures. In the first stage of data evaluation, the reaction rate coefficient k_1 was varied by taking different literature values from [1, 3, 5]. Later, to obtain better agreement with the experiments, the reaction rate coefficient k_1 is varied by keeping values of either A or E fixed. A rate coefficient equal to $1.5 \times 10^{13} \text{ cm}^6 \text{ mol}^{-2} \text{ s}^{-1}$ with an activation energy of 25 kJ mol^{-1} was found to give the best representation of the experimental data. As seen in Figure 6, the experimentally obtained peak concentrations vary almost linearly with temperature within the 1400–2600 K range. Here, a smooth curve is not seen (and not expected) because the individual experiments are taken at varying pressure behind the reflected shock wave (p_5 varies between 0.85–1.4 bar). The simulations, however, are performed for the individual experimental temperature T_5 and corresponding pressure p_5 values. The temperature dependence of all four mixtures is very well reproduced by the simulations in the entire temperature range. As shown in

Figure 6 at lower temperatures, where the agreement between the experimental values and simulation are not clearly seen on this scale, the calculated OH* is within 10% compared to the measured value. The prediction of OH* concentrations with k_1 from literature using the hydrogen kinetics scheme from this study is compared to the measured OH*. Hidaka et al. [3] determined k_1 in a temperature range similar to our study where their k_1 was found to be about 70% lower than our prediction. The predicted OH* concentrations at the peak maximum with their k_1 were about 60% lower compared to our measurements. The quenching rate coefficient k_3 of the major efficient collider ($M = H_2O$) is about 50% lower in their kinetics scheme compared to ours. Thus, recalculating the rate coefficient of Hidaka et al. for major quencher corrections would require about 50% higher rate coefficients, giving rates closer to our prediction. When the OH* concentration is calculated with the rate coefficients k_1 from Hall et al. [5] and the temperature-independent rate coefficient from Smith et al. [1] it is seen that at intermediate temperatures (1500–2200 K) the calculated OH* concentrations are about 8 and 4 times higher than the absolute OH* concentration maxima measured in this work. At very high temperatures (2800–3000 K) the predicted OH* concentrations from Smith et al. and Hall et al. data are similar to the present work since their formation is independent of k_1 . However, they are closer to the measurements at temperatures near 1000 K. The deviation of the OH* prediction at intermediate temperatures with k_1 from [1] is likely due to the fact that it was derived by fitting flame measurements at about 1000 K. When Petersen et al. measured k_1 at 1000–1800 K [34], an increase in the rate coefficient by one order of magnitude was required to fit the measured OH* profiles compared to their later study at temperature range of 1200–2200 K [5]. Therefore, a lower rate coefficient is required at higher temperatures compared to the one near 1000 K. Thus, OH* concentrations predicted by [1] and [5] are higher compared to those simulated based on the reaction rate coefficient determined from our study for the intermediate temperature conditions of Figure 6.

The uncertainty in the rate coefficient k_1 can be divided into systematic and statistical contributions.

The determination of k_1 depends on the absolute [OH*] concentrations and thus on the calibration.

An evaluation showed that any error in the calibration factor affects the resulting k_1 values

by the same magnitude. The $\pm 20\%$ error in the calibration strategy, therefore, leads to a systematic error in k_1 of $\pm 20\%$. Additional systematic errors can be connected to the quenching rate coefficients. The quenching rate with Ar as a main collider has a small effect on the prediction of the OH* concentrations while the uncertainties in the quenching cross sections of H₂O causes an additional systematic error of 3% on k_1 . This value was obtained by varying k_3 (for M = H₂O) within the 8% uncertainty of the quenching cross section stated by Cattolica et al. [35].

In the data analysis each individual experiment directly leads to the determination of a k_1 value. A statistical error of $\pm 15\%$ ($1-\sigma$) was derived from the scatter in k_1 results that are evaluated from the total of 20 individual measurements at different temperatures and mixture compositions. The influence of the 5–15 K uncertainty in the determination of the gas temperature was considered and it was found to be negligible compared to the other uncertainties. The errors are combined as the square root of the sum, including all of the uncertainties in the determination of the k_1 values. The overall uncertainty in k_1 could be as high as 30%.

In order to validate our rate coefficient (k_1) additional numerical experiments were done with the maximum intensity plotted against temperature from Figure 1 in Hall et al. [5]. A good match is achieved with our rate coefficient (cf. Figure 9). This figure also shows a similar comparison with simulations based on the GRI-mech version 3.0 [36] as a base mechanism for hydrogen oxidation using k_1 from this work. The results although deviates slightly from our hydrogen mechanism but are however in agreement with the measurements.

The various rate coefficients for k_1 from different references are shown in an Arrhenius plot in Figure 8. Our rate coefficient is slightly higher than the rate coefficient suggested by Hidaka et al. [3] and lower than others. The plot shows literature data of experimental measurements of k_1 over the temperature range of 1000–2000 K. The highest rate coefficient (Hall et al. [5]) and the lowest one (Hidaka et al. [3]) differ by two orders of magnitude. This difference reflects the difficulty in evaluating the OH* formation rate coefficient k_1 from measurements. The determination of rate coefficients is affected by the uncertainty of the kinetics model in addition to the measurement

errors described previously. The calibration of the OH* measurements is based on predictions of the concentrations of the intermediates such as H and O atoms from which OH* is formed. The uncertainty of the different kinetics models is reported to be below 20% [37]. Uncertainties of the ground state precursors of OH* impact the prediction of OH* and affects therefore the determination of k_1 . As an example, a change in the rate coefficient of reaction $\text{H} + \text{O}_2 = \text{OH} + \text{O}$ by $\Delta \log k = \pm 0.2$ (maximum recommended limit in [26]) altered the OH* peak concentrations by $\pm 10\%$ in a lean $\text{H}_2/\text{O}_2/(98\%)$ Ar mixture at 1200 K and 1.4 bar. Although this uncertainty would not affect the temperature dependence corresponding to the activation energy E , it would influence the determination of the pre-exponential factor which is adjusted to achieve the best fit with the measurements to obtain k_1 .

The recommended reaction rate coefficient k_1 in the present work is further tested against shock-tube measurements of the ignition delay based on OH* and published data for one-dimensional laminar flames [1, 27] and will be discussed in the next section.

Shock tube measurements and 0-D modeling

A homogeneous closed reactor model (0-D) allows the simulation of time-dependent processes in a homogenous reaction system that reproduces the induction time and the temporal variation of chemiluminescence signals in a shock tube [32]. In order to validate the mechanism of OH* formation discussed in the present work in hydrogen combustion (Table 2), a well established procedure of comparing simulated and experimentally determined ignition delay time is performed. In the present work the ignition delay time τ corresponds to the time when the tangent to the maximum slope of the OH* concentration profile intersects the time axis. Clearly, the ignition delay time is governed by the kinetics of the ground state chemistry and is not depending on (R1). The most sensitive reactions affecting the ignition delay times are the chain-branching reactions (R7) and (R8). However, when reaction pathways leading to OH* other than (R1) are considered, no consensus between simulation and experiment is observed in terms of ignition delay times.

Therefore, the ignition delay time measurements will serve mainly as an additional check for the ground state chemistry.

The important pathways through which OH* is formed are discussed in an integral reaction flow analysis. In order to get insight into rate-limiting reactions important to OH* during induction phase, a global sensitivity analysis is presented and discussed in this section.

Ignition delay time: Calculations of ignition delay times are performed for the given set of experimental conditions for H₂/O₂ mixtures diluted in argon and nitrogen (Table 1). The experimental data correspond to lean ($\phi = 0.5$) and stoichiometric conditions. In our experiments the reflected shock temperature T_5 ranges from 1400–3000 K with pressure p_5 ranging from 0.85 to 1.40 bar. Although sparse literature data can be found for these experimental conditions only, comparable ignition delay time measurements can be found in Skrebkov et al. [7]. They investigated the ignition delay of various highly diluted, stoichiometric hydrogen/oxygen mixtures in a shock tube within a comparable pressure range. One of their mixtures, namely 0.93% O₂ + 1.87% H₂ in Ar, is quite comparable to the measurements presented in this paper. The measurements in [7] cover a wider pressure range ($0.5 \text{ bar} < p_5 < 1.7 \text{ bar}$) than the measurement presented here (Table 1).

Figure 10 shows the comparison of simulated and experimental ignition delay times at the above mentioned conditions. The simulations are performed at the given experimental conditions shown by line. The lean mixture A corresponds to 98% argon dilution and C with 5% N₂ and 93% argon. Mixture B corresponds to stoichiometric mixtures with argon dilution of 97% whereas mixture D contains 5% N₂ and 92% argon as diluents. As can be seen from Figure 10, the simulated ignition times are in very good agreement with the measurements at corresponding conditions. The ignition delay times obtained from Ar-diluted and Ar + N₂-diluted mixtures are very close to each other. The slope of the experimental and simulated data matches very well such that the activation energy of ignition was reproduced.

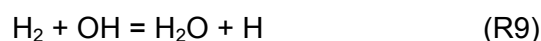
As it was seen in an earlier section, the peak concentrations of OH* are a function of the OH* formation reaction (R1) whereas the ignition delay time is dependent on ground state chemistry. It is then assumed that the selection of the rate coefficient of reaction (R1) has no influence on the calculation of ignition delay. However, we have observed that the choice of reaction forming OH* other than (R1) may result in differences of the simulated OH* compared to the OH* signal variation that is used to derive τ . For example, formation of OH* from reaction (R5) [6] is discussed earlier in this paper. We incorporated this reaction in the mechanism along with reaction (R1). Figure 11 shows the OH* concentration profile with and without the above mentioned reaction (R5) incorporated in the calculation along with the reaction (R1) at three different temperatures at $\phi = 0.5$. Implementing reaction (R5) with reaction (R1) in the OH* sub-scheme forms a dual peak in the OH* profile. The first peak results from the reaction (R5) followed by the second peak caused by reaction (R1). The OH* resulting from reaction (R5) is formed in the induction phase where H₂ and HO₂ concentrations are high. At temperatures below 1600 K, the recombination reaction (R1) is dominant. However, the first peak is prominent at temperatures above 1600 K which is also true at stoichiometric and rich fuel conditions. With the reaction (R5) included in the mechanism (shown in Figure 12), above 1600 K the simulated ignition delay times (obtained at first rise in OH* profile) were much shorter than the measured ones. In [8] dual peaks in the measured OH* emission were observed in only three experiments. In addition, the geometric mean of two calculated OH* maxima of the dual peaks in [8] – similar to that depicted in Fig 10 (open square) – were compared with the measurements. In the present work, no dual peaks were observed in the measured emission profiles. Thus, this result supports that reaction (R1) is a dominant source for OH* formation.

OH* formation pathways: An integral reaction flow analysis explains the relative rate of formation and consumption of species (here OH*) from different reactions in the course of reaction time. The formation path of OH* in hydrogen mixtures from the three body recombination reaction (R1) is mainly followed by the fuel and oxidizer decomposition. Under homogeneous conditions H atoms are formed by the chain branching reaction $\text{H}_2 + \text{O} \rightarrow \text{OH} + \text{H}$ (R8) and the exothermic chain propagation reaction $\text{H}_2 + \text{OH} \rightarrow \text{H}_2\text{O} + \text{H}$ (R9). The basic chain branching reaction $\text{O}_2 + \text{H} \rightarrow \text{OH}$

+ O (R7) is the major source of O atoms (90%) ranging from 99 to 70% consumption of O₂ in fuel rich to lean condition at 1 bar. The OH* concentration formed from these species is small compared to the concentration of the major species and has no influence on the basic hydrogen oxidation chemistry. The consumption of OH* is dominated by the quenching reaction (R3) with M = H₂O, H and Ar. The reaction flow analysis shows the formation of OH* through reaction (R1) as a result of reactions (R7) to (R9) in which H and O atoms are formed.

Sensitivity analysis: A global sensitivity analysis with respect to OH* is performed to understand the rate-limiting reactions that are important for the OH* formation during the induction phase. Figure 13 shows the analysis performed for lean ($\phi = 0.5$) and stoichiometric H₂/O₂/Ar mixtures at atmospheric pressure and 2300 K (highest attained flame temperature with Ar dilution) at the first part of the induction period up to 29 μ s (lean) and 30 μ s (stoichiometric). The sensitivity coefficients were calculated by forming partial derivatives of the OH* concentration with respect to the rate coefficients at constant time. The coefficients computed are normalized to the maximum ones and only sensitivities higher than 5% are considered. The sensitivity analysis was also performed for the above shock-tube conditions with 97% argon dilution at different equivalence ratios and flame temperatures.

The basic chain branching step O₂ + H, forming OH and O species (R7), is found to be most sensitive (positive) under the conditions investigated, also for stoichiometric and fuel-rich conditions. The formation of OH* strongly depends on the rate of this reaction which is a well-known reaction with reaction rate coefficients known over a wide temperature range [26]. Besides, relevant reactions with significant positive sensitivity are as follows:



At higher flame temperatures only OH* quenching reactions (M = O₂, H₂, Ar) contribute

to very low negative sensitivity. As it is seen in the Arrhenius plot (Figure 1) of the quenching reactions the literature value of rate coefficients are in good agreement with each other. From the sensitivity analysis it is seen that the reaction kinetics of OH* is determined by the important chain branching reaction (R7) along with reactions (R8), (R9) and (R11).

Premixed laminar flame (1-D) modeling

Absolute concentrations measured in flames provide a stringent test on kinetics mechanisms. The above sensitivity analysis showed that the reactions consuming and producing H, O and OH are most influential to the OH* formation. A 1-D simulation of a premixed burner-stabilized laminar flame was performed to get information on these species in hydrogen combustion. The absolute concentrations of these species were calculated for the conditions investigated by Vandooren et al. [27]. They measured major radicals and stable species concentrations at low pressure (0.05 bar) in fuel-rich ($\phi = 1.91$) flames by molecular beam mass spectrometry. Figure 14 presents a comparison of measured and simulated species profiles as a function of distance above the burner surface. The simulated concentration profiles of the species important with respect to reaction (R1) are in close agreement with the measurements. The burner-stabilized flame calculation showed that the H and O concentrations are well predicted with deviations of +2% and +20% compared to the measurements, respectively. A measurement error of 10% has been estimated for H- and O-atom concentrations in [27]. This comparison was intended to provide an understanding of the relevance of H and O concentrations for the prediction of OH* in flames.

Absolute OH* concentration: Recently, Smith et al. [1] measured absolute OH* concentrations in premixed hydrogen/air flames. Our recommended rate coefficient for reaction (R1) in the present work was applied in the mechanism to perform a burner-stabilized one-dimensional laminar hydrogen-air flame calculation for the experimental conditions of [1] (0.05 bar, $\phi = 1.54$). The spatial profile of measured OH* emission is presented in their work. The peak OH* number density

was 2.2×10^6 molecules cm^{-3} at 5.6 mm above the burner surface. In our calculations H-atom recombination at the burner surface was considered and the measured temperature profile and gas flow rate was used as an input to account for the heat loss of the burner-stabilized flame.

Figure 15 presents the absolute OH* concentration calculated in the present work along with the measurements [1]. The shape of the measured OH* concentration profile as a function of height above the burner is well predicted by the calculation. The peak OH* concentration calculated with the reaction rate coefficient k_1 recommended in the present work is 8.8×10^5 molecules cm^{-3} which is 2.4 times lower than the measured value. Its peak is located 4.7 mm above the burner surface, a difference of 0.9 mm to the measured position. Additional calculations were done with other rate coefficients from the literature for reaction (R1). The rate coefficient suggested by Smith et al. [1] and Hall et al. [5] predict the OH* concentration 2.6 and 1.3 times higher than the measured value, respectively. GRI-mech 3.0 [36] is used as a base model in both works. At this flame condition the rate coefficient recommended by [5] well reproduces the measurements. The model discrepancy between the prediction of OH* by using k_1 from [1] in present work from their own is due to the differences in prediction of H- and O- atom concentrations. As an example, at Vandooren et al. flame condition, H-atom and O-atom concentrations with GRI-mech 3.0 [36] are predicted 15% and 45% lower than the measurements whereas with base model from present work they are 2% and 20% higher respectively. The uncertainty of such H-, O- atom prediction affects k_1 derived by [1]. Therefore, when k_1 from [1] is used in present work, the differences in H-atom + O-atom concentrations from both mechanisms are added leading to over prediction of about a factor of 2 .

Although more OH* flame measurements for further validation would be required, the above flame calculation implies that the rate coefficient determined in the present work (in the temperature range of 1400–2800 K) is 2.5 times slower than the measurements at the present flame temperature of about 1100 K.

Conclusions

The kinetic behavior of the OH* formation by the major forming reaction $\text{H} + \text{O} + \text{M} = \text{OH}^* + \text{M}$ (R1) is studied by detailed kinetics modeling and compared to shock-tube experiments at temperatures between 1400–3300 K and pressures of 1 bar. Based on the comparison of the temperature dependence of reaction (R1) by measured emission and computed concentration, a reaction rate coefficient of $(1.5 \pm 0.4) \times 10^{13} \exp(-25 \text{ kJmol}^{-1}/RT) \text{ cm}^6\text{mol}^{-2}\text{s}^{-1}$ is determined. Based on the knowledge that the main reaction channel leading to OH* at temperatures above 2800 K is the reverse of the well-described quenching reaction (R3) it was possible to link the OH* chemiluminescence intensities to the respective concentrations and then used this calibration for quantification of OH* concentrations at lower temperatures. The application of this calibration in stoichiometric and lean $\text{H}_2/\text{O}_2/(\text{Ar}, \text{N}_2)$ mixtures yielded a good agreement between measurements and the simulations using the updated rate coefficient for reaction (R1). A sensitivity analysis with respect to OH* formation is performed under homogeneous conditions and it is found that the OH* formation is very sensitive to the important basic chain branching reaction $\text{O}_2 + \text{H} = \text{OH} + \text{O}$. In burner-stabilized flames the absolute concentrations of H and O atoms, important for OH* formation, are well reproduced for the experimental conditions of Vandooren et al. [27]. The prediction for k_1 mainly depends on the OH* precursor prediction (i.e. H-, O-atom concentrations) of the kinetics model studied. Therefore, any uncertainties in these species will impact the accuracy of k_1 . Because experimental flame measurements of H- and O-atom concentrations over a wide temperature are scarce, it is difficult to find out the performance of the different kinetics schemes with respect to these precursors. However, related to the present study we estimate a 20% uncertainty at about 1100 K from our kinetics scheme while considering the rate k_1 from present work. Taking this into account along with the recommended rate coefficient of reaction (R1) the absolute peak OH* concentration is found in fairly good agreement with the number density of OH* measured in premixed flames by Smith et al. [1].

Acknowledgments

The authors are grateful to Prof. Ulrich Maas (University of Karlsruhe) for providing us with his INSFLA code. They thank Dr. Greg Smith (SRI, Menlo Park) for valuable discussions. Financial support from the Deutsche Forschungsgemeinschaft (German Research Foundation, DFG) is gratefully acknowledged.

Appendix

The hydrogen kinetics scheme discussed in this paper is validated for the predictions of ignition delay times, flame velocities and flame structures at various conditions.

The kinetics scheme discussed in Heghes 2007 [25] has been modified in the current work, which is presented in Table 1. The underlying mechanism originating from Heghes 2007 [25] has considered reaction rate of $\text{H} + \text{O}_2 + \text{M} = \text{HO}_2 + \text{M}$ (R14) as a sum of two Arrhenius expression. The present study considers only one reaction rate (R14) as shown in Table 2. The reaction $\text{H} + \text{O}_2 = \text{OH} + \text{O}$ (R7) is the basic chain branching reaction at high temperature and the flame propagation is highly sensitive to this reaction. (R14), thus, competes with reaction (R7) at the given temperature and pressure conditions.

Ignition delay times

Ignition delay times at high temperatures are discussed in the paper. However, here we present the prediction of ignition at the second explosion limit. At temperatures below 1025 K the experimental condition approaches the second explosion limit. At this temperature range, the rate of combustion is determined by the competition of the chain branching and chain terminating

reactions in the gas phase. In our mechanism the rate of the second important chain branching reaction $O + H_2 = OH + H$ (R8) was considered from the recent recommendation of Baulch et al. 2005 [26]. Although this rate is similar to their earlier prediction at high temperature (Baulch et al. 1994 [30]), it deviates significantly at lower temperatures. The ignition delay times at lower temperatures are calculated for comparison with both rates in the figures below.

Figure 16 shows the ignition delay times measured by Slack [38] at 2 bar in stoichiometric H_2 /air mixtures. The measured ignition delay time, τ is defined as the time interval between the reflected shock pressure rise and maximum positive change of the OH^* emission signal. Because our model predicts OH^* , the ignition delay time is predicted from the maximum slope of the OH^* concentration profile. The model prediction of the present work reproduces the ignition delay at temperatures higher than 1060 K. However, at lower temperatures, predicted ignition delays are approximately 2 times shorter than measured ones. The prediction of ignition delay times with the older rate k_8 (Baulch 1994 [30]) is similar to the newer rate (Baulch 2005 [26]). From the figure it is clear that only the Conaire et al. mechanism [31] shows a better agreement with the measured ignition delay at lower temperatures.

Similarly, Skinner and Ringrose [39] and Schott and Kinsey [40] measured the ignition delay times of the hydrogen mixtures at lower temperatures. In both studies, the experimental data are plotted as product of ignition measured from the maximum OH signal and initial oxygen concentration. As shown in Figure 17, the prediction of the present mechanism is similar to the predictions of the Konnov version 0.3 [41] mechanism and are in good agreement with the measurements of Schott and Kinsey [40]. Good agreement is seen at lower temperature between the present simulation and the measurement of Skinner and Ringrose [39] (Figure 18). The measurements show shorter ignition delay than the predictions based on the mechanism from Konnov et al. [41], Mueller et al. [42], and Conaire et al. [31]. In both figures 17 and 18, the ignition delay times predicted with the $H + O_2$ rate coefficient from [30] is similar to the one from present study.

Flame velocity

Figure 19 presents various reported values of laminar flame velocity measurements for H₂/air mixtures at 1 bar and 298 K initial temperature. The older reported values correspond to the flame velocity without flame stretch correction. The recent measurements of Aung et al. [43], Taylor [44], Vagelopoulos et al. [45], and Wu and Law [46] were corrected for flame stretch. The prediction based on our mechanism agrees well with the new measurements of Taylor over the entire measurement range. At low H₂ mixture fractions they agree well with the measurements of Aung et al. [43], Vagelopoulos et al. [45], and Wu and Law [46]. The simulated flame velocity presented in Heghes 2007 [25] is shown for reference.

References:

1. G. Smith; C. Park; J. Luque, *Combust. Flame* 140 (2005) 385-389
2. W. Kaskan, *J. Chem. Phys.* 31 (1959) 944-956
3. Y. Hidaka; S. Takahashi; H. Kawano; M. Suga; W. C. Gardiner, Jr., *Int. J. Chem. Phys.* 86 (1982) 1429-1433
4. T. Koike; K. Morinaga, *Bull. Chem. Soc. Jpn.* 55 (1982) 52-54
5. J. M. Hall; E. L. Petersen, *Int. J. Chem. Kinet.* 38 (2006) 714-724
6. O. Skrebkov; Y. Myagkov; S. Karkach; V. Vasilev; A. Smirnov, *Dok. Phys. Chem.* 383 (2002) 93-96
7. O. Skrebkov; S. Karkach; V. Vasilev; A. Smirnov, *Chem. Phys. Letts.* 375 (2003) 413-418
8. G. Smekhov; L. Ibraguimova; S. Karkach; O. Skrebkov; O. Shatalov, *High Temperature* 45 (2007) 395-407
9. A. Burcat; B. McBride, *Aerospace Engineering Report*, TAE 804 (1997)
10. D. Gutman; R. Lutz; N. Jacobs; E. Hardwidge; G. Schott, *J. Chem. Phys.* 48 (1968) 5689-5694
11. C. Marques; L. Benvenuti; C. Bertran, *J. Braz. Chem. Soc.* (2006) 302-315
12. P. Paul; J. Durant; J. Gray; M. Furlanetto, *J. Chem. Phys.* 102 (1995) 8378-8384
13. A. G. Gaydon, *The spectroscopy of flames*, Wiley, New York, 1974.
14. P. W. Fairchild; G. P. Smith; D. R. Crosley, *J. Chem. Phys.* 79 (1983) 1795-1807
15. B. L. Hemming; D. R. Crosley; J. E. Harrington; V. Sick, *J. Chem. Phys.* 115 (2001) 3099-3104
16. A. E. Bailey; D. E. Heard; P. H. Paul; M. J. Pilling, *J. Chem. Soc., Faraday Trans.* 93 (1997) 2915-2920
17. K. H. Becker; D. Haaks; T. Tatarczyk, *Chem. Phys. Let.* 24 (1974) 564-567
18. D. E. Heard; D. A. Henderson, *Phys. Chem. Chem. Phys.* 2 (2000) 67-72
19. B. L. Hemming; D. R. Crosley, *J. Phys. Chem. A* 106 (2002) 8992-8995
20. J. B. Jeffries; K. Kohse-Höinghaus; G. P. Smith; R. A. Copeland; D. R. Crosley, *Chem. Phys. Let.* 152 (1988) 160-166

21. M. Tamura; P. A. Berg; J. E. Harrington; J. Luque; J. B. Jeffries; G. P. Smith; D. R. Crosley, *Combust. Flame* 114 (1998) 502-514
22. R. J. Kee; F. M. Rupley; J. A. Miller; M. E. Coltrin; J. F. Grcar; E. Meeks; H. K. Moffa; A. E. Lutz; G. Dixon-Lewis; M. D. Smooke; J. Warnatz; G. H. Evans; R. S. Larson; R. E. Mitchell; L. R. Petzold; W. C. Reynolds; M. Carcotsis; W. E. Stewart; P. Glarborg; C. Wang; O. Adigun, CHEMKIN Collection, Release 3.6, Reaction Design, Inc., San Diego CA (2000)
23. D. Davidson; M. Roerig; E. L. Petersen; M. D. D. Rosa; R. K. Hanson, *J. Quant. Spectrosc. Radiat Transfer* 55 (1996) 755-762
24. J. Warnatz; U. Maas; R. W. Dibble, *Combustion*, Springer-Verlag, Berlin Heidelberg, New York, 2006.
25. C. I. Heghes. C1-C4 Hydrocarbon Oxidation Mechanism. University of Heidelberg: <http://reaflow.iwr.uni-heidelberg.de/doctoral.html>, 2007.
26. D. L. Baulch; C. T. Bowman; C. J. Cobos; R. A. Cox; T. Just; J. A. Kerr; M. J. Pilling; D. Stocker; J. Troe; W. Tsang; R. W. Walker; J. Warnatz, *J. Phys. Chem. Ref. Data* 34 (2005) 757-1397
27. T. Vandooren; J. Bian, *Proc. Comb. Symp.* 23 (1991) 341-346
28. G. Smith; J. Luque; C. Park; J. Jeffries; D. Crosley, *Combust. Flame* 131 (2002) 59-69
29. D. R. Stull; H. Prophet, *Nat. Stand. Ref. Data Ser., Nat. Bur. Stand. (U.S.)* 2nd Edition (1974) 37
30. D. L. Baulch; C. J. Cobos; R. A. Cox; P. Frank; G. Hayman; T. Just; J. A. Kerr; T. Murrells; M. J. Pilling; J. Troe; R. W. Walker; J. Warnatz, *Combustion and Flame* 98 (1994) 59-79
31. M. Conaire; H. Curran; J. Simmie; W. Pitz; C. Westbrook, *Int. J. Chem. Kinet.* 36 (2004) 603-622
32. U. Maas; J. Warnatz, *Combust. Flame* 74 (1988) 53-69
33. U. Maas, *Applications of Mathematics* 40 (1995) 249-266
34. E. L. Petersen; D. M. Kalitan; M. J. Rickard, 39th AIAA Joint Propulsion Conference and Exhibit AIAA 2003-4493 (2003)
35. R. J. Cattolica; T. G. Mataga, *Chem. Phys. Lett.* 182 (1991) 623-631
36. G. P. Smith; D. M. Golden; M. Frenklach; N. W. Moriarty; B. Eiteneer; M. Goldenberg; C. T. Bowman; R. K. Hanson; S. Song; W. C Gardiner, Jr.; V. V. Lisianski; Z. Qin, http://www.me.berkeley.edu/gri_mech, (1999)
37. K. Kohse-Hoeinghaus; J. Jeffries, *Applied Combustion Diagnostics*, Taylor & Francis, New York (2002) 511
38. M. W. Slack, *Combust. Flame* 28 (1977) 241-249
39. G. B. Skinner; G. H. Ringrose, *J. Chem. Phys.* 42 (1965) 2190-2192
40. G. L. Schott; J. L. Kinsey, *J. Chem. Phys.* 29 (1958) 1177-1182
41. A. A. Konnov mechanism, <http://homepages.vub.ac.be/~akonnov>, (1998)
42. M. A. Mueller; R. A. Yetter; F. L. Dryer, *Int. J. of Chem. Kinet.* 31(1999) 113-125
43. K. T. Aung; M. I. Hassen; G. M. Faeth, *Combust. Flame* 109 (1997) 1-24
44. S. C. Taylor, Ph.D Thesis, University of Leeds (1991)
45. C. M. Vagelopoulos; F. N. Egolfopoulos; C. K. Law, *Proc. Combust. Inst.* 25 (1994) 1341-1347
46. C. K. Wu; C. K. Law, *Proc. Combust. Inst.* 20 (1984) 1941-1949
47. J. Warnatz, *Ber. Bunsenges. Phys. Chem.* 82 (1978) 643

Tables:

Table 1: Mixture composition of the four test mixtures and pressure and temperature ranges of the shock-tube experiments

Mixture	ϕ	Composition	T_5 range / K	p_5 range / bar
A	0.5	1% H ₂ + 1% O ₂ in Ar	1400 – 3300	0.85 – 1.50
B	1.0	2% H ₂ + 1% O ₂ in Ar	1440 – 3180	0.90 – 1.40
C	0.5	1% H ₂ + 1% O ₂ + 5% N ₂ in Ar	1400 – 3200	0.90 – 1.40
D	1.0	2% H ₂ + 1% O ₂ + 5% N ₂ in Ar	1450 – 3200	0.90 – 1.45

Table 2: Reaction kinetics scheme of hydrogen oxidation along with the OH* sub-scheme.

Reaction rate coefficient $k = AT^n \exp(-E/RT)$. The collision efficiencies used in the mechanism [24] are given below:

No.	Elementary reaction	A / cm, mol, s	n	E / kJmol ⁻¹	Reference
H₂/O₂ kinetics scheme					
R7	O ₂ + H = OH + O	2.06E+14	-0.097	62.85	[26]
R8	H ₂ + O = OH + H	3.82E+12	0.0	33.26	[26]
		1.02E+15	0.0	80.23	
R9	H ₂ + OH = H ₂ O + H	2.17E+08	1.52	14.47	[26]
R10	OH + OH = H ₂ O + O	3.35E+04	2.42	-8.06	[26]
R11	H + H + M(1) = H ₂ + M(1)	1.02E+17	-0.6	0.00	[26]
R12	O + O + M(1) = O ₂ + M(1)	5.40E+13	0.0	-7.40	[25]
R13	H + OH + M(2) = H ₂ O + M(2)	5.56E+22	-2.0	0.00	[26]
R14	H + O ₂ + M(3) = HO ₂ + M(3)	1.75E+17	0.0	0.00	[26]
	low	2.37E+19	-1.2	0.00	
	Troe	0.5 0.0	0.0	0.00	
R15	HO ₂ + H = OH + OH	4.46E+14	0.0	5.82	[26]
R16	HO ₂ + H = H ₂ + O ₂	1.05E+14	0.0	8.56	[26]
R17	HO ₂ + H = H ₂ O + O	1.44E+12	0.0	0.00	[26]
R18	HO ₂ + O = OH + O ₂	1.63E+13	0.0	-1.86	[26]
R19	HO ₂ + OH = H ₂ O + O ₂	9.28E+15	0.0	73.25	[26]

R20	$\text{HO}_2 + \text{HO}_2 = \text{H}_2\text{O}_2 + \text{O}_2$	4.22E+14 1.32E+11	0.0 0.0	50.14 -6.82	[26]
R21	$\text{OH} + \text{OH} + \text{M}(1) = \text{H}_2\text{O}_2 + \text{M}(1)$ low Troe	1.57E+13 5.98E+19 0.5 0.0	0.0 -0.8 0.0	0.00 0.00 0.00	[26]
R22	$\text{H}_2\text{O}_2 + \text{H} = \text{H}_2 + \text{HO}_2$	1.69E+12	0.0	15.71	[26]
R23	$\text{H}_2\text{O}_2 + \text{H} = \text{H}_2\text{O} + \text{OH}$	1.02E+13	0.0	14.97	[26]
R24	$\text{H}_2\text{O}_2 + \text{O} = \text{OH} + \text{HO}_2$	4.22E+11	0.0	16.63	[26]
R25	$\text{H}_2\text{O}_2 + \text{O} = \text{H}_2\text{O} + \text{O}_2$	4.22E+11	0.0	16.63	[26]
R26	$\text{H}_2\text{O}_2 + \text{OH} = \text{H}_2\text{O} + \text{HO}_2$	1.64E+18 1.92E+12	0.0 0.0	123.05 1.79	[26]
OH* sub-scheme					
R1	$\text{H} + \text{O} + \text{M}(1) = \text{M}(1) + \text{OH}^*$	1.50E+13	0.0	25.0	Present work
R2	$\text{OH}^* = \text{OH} + h\nu$	1.45E+06	0.0	0.0	[28]
R3,1	$\text{OH}^* + \text{O}_2 = \text{OH} + \text{O}_2$	2.10E+12	0.5	-2.0	[21]
R3,2	$\text{OH}^* + \text{H}_2\text{O} = \text{OH} + \text{H}_2\text{O}$	5.93E+12	0.5	-3.6	[21]
R3,3	$\text{OH}^* + \text{H}_2 = \text{OH} + \text{H}_2$	2.95E+12	0.5	-1.9	[21]
R3,4	$\text{OH}^* + \text{N}_2 = \text{OH} + \text{N}_2$	1.08E+11	0.5	-5.2	[21]
R3,5	$\text{OH}^* + \text{OH} = \text{OH} + \text{OH}$	6.01E+12	0.5	-3.2	[21]
R3,6	$\text{OH}^* + \text{H} = \text{OH} + \text{H}$	1.31E+12	0.5	-0.7	[21]
R3,7	$\text{OH}^* + \text{Ar} = \text{OH} + \text{Ar}$	1.69E+12	0.0	17.3	[12]

With:

$$\text{M}(1) = [\text{H}_2] + 6.5[\text{H}_2\text{O}] + 0.4[\text{O}_2] + 0.4[\text{N}_2] + 0.35[\text{Ar}]$$

$$\text{M}(2) = [\text{H}_2] + 2.5[\text{H}_2\text{O}] + 0.4[\text{O}_2] + 0.4[\text{N}_2] + 0.15[\text{Ar}]$$

$$\text{M}(3) = [\text{H}_2] + 6.5[\text{H}_2\text{O}] + 0.4[\text{O}_2] + 0.4[\text{N}_2] + 0.29[\text{Ar}]$$

Figures:

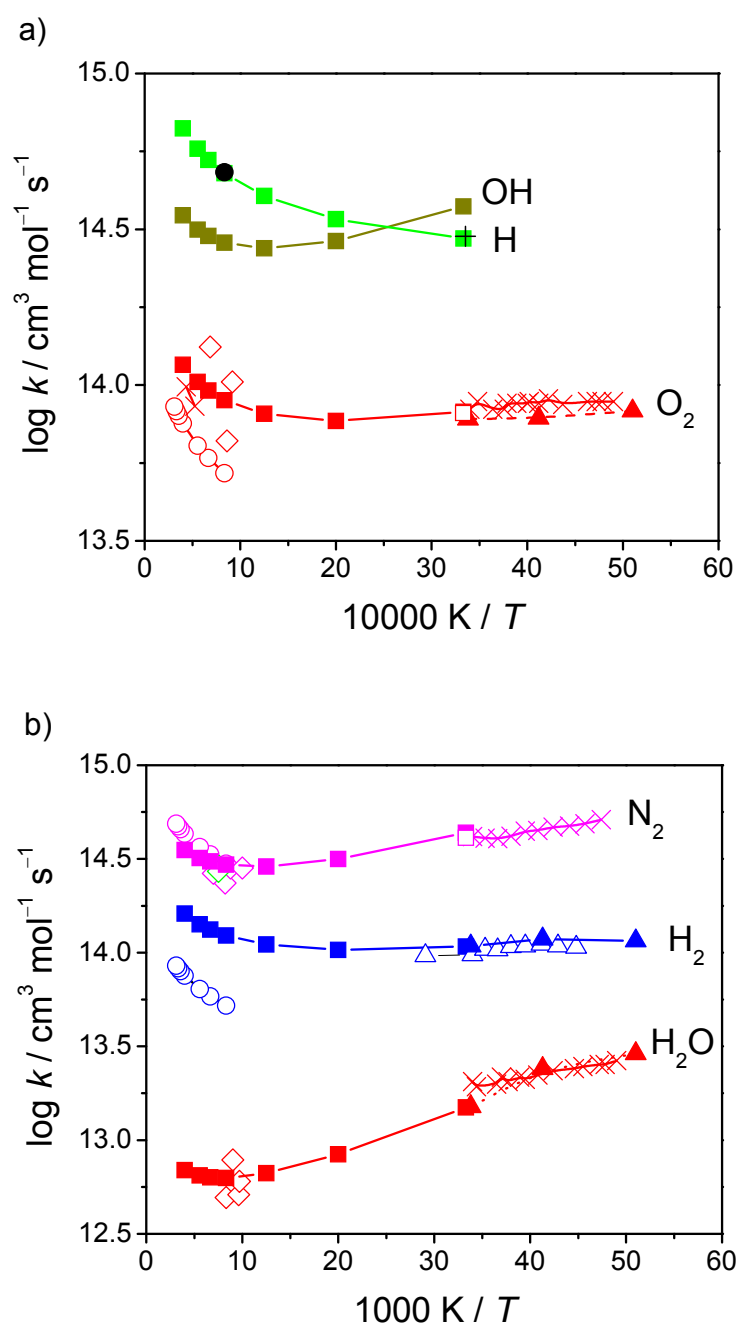


Figure 1 : Arrhenius plot of the OH* quenching reaction (R3) with third partner $M = \text{O}_2, \text{H}, \text{OH}$ (plot a); $M = \text{N}_2, \text{H}_2, \text{H}_2\text{O}$ (Plot b). Symbols: \diamond Fairchild et al. [14]; \blacksquare Tamura et al. [21]; \times Bailey et al. [16]; \square Hemming et al. [15]; \blacktriangle Hemming et al. [19]; \circ Hidaka et al. [3]; \triangle Heard et al. [18]; $+$ Becker et al. [17]; \bullet Jeffries et al. [20].

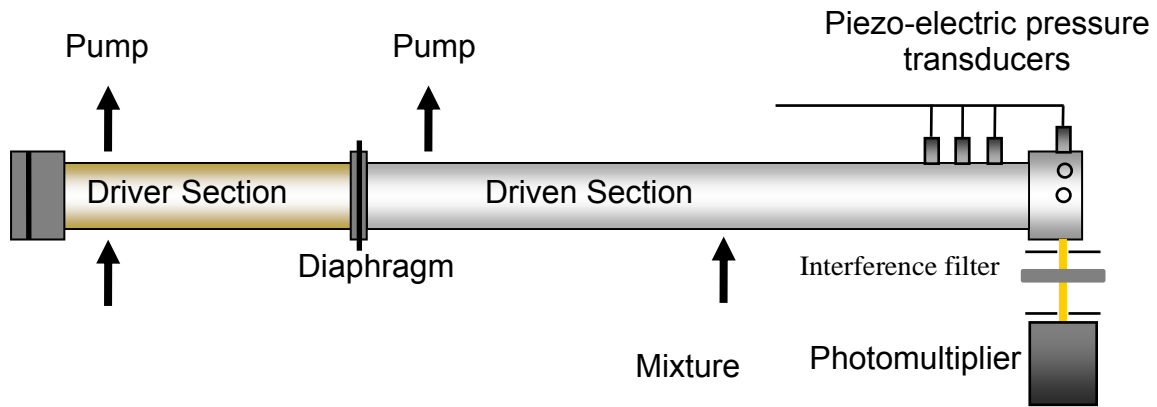


Figure 2: Schematic setup of the shock tube

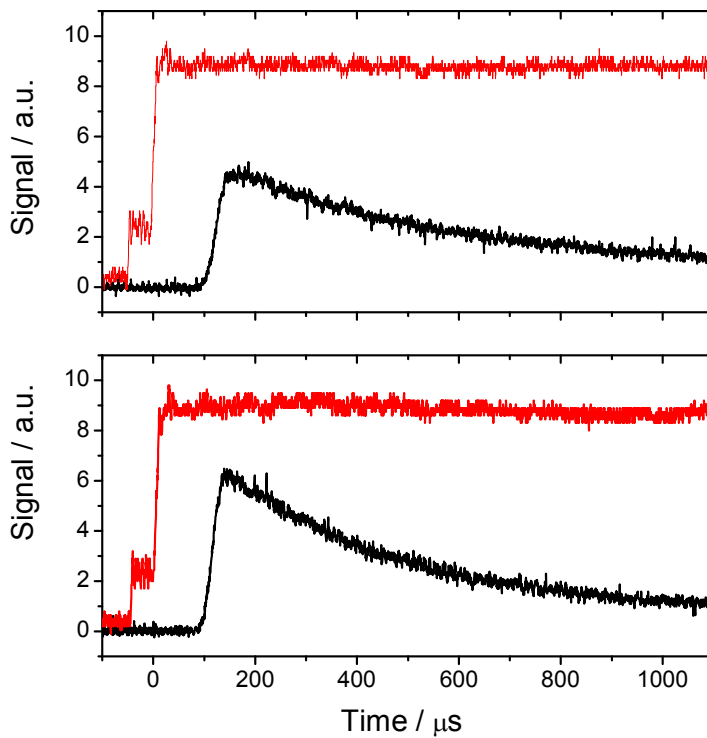


Figure 3: Pressure and OH* emission signal during the ignition of a mixture of 1% O₂ + 1% H₂ in Ar at $p_5 = 1.20$ bar and $T_5 = 1674$ K (upper curve) and of a mixture of 1% O₂ + 2% H₂ in Ar at $p_5 = 1.15$ bar and $T_5 = 1622$ K (lower curve). The step due to reflected shock arrival is defined as t_0 . For determination of the ignition delay time ($\tau = 88$ μ s, e.g. for the lean mixture) the steepest increase

in OH*-chemiluminescence signal is taken and extrapolated to the zero level.

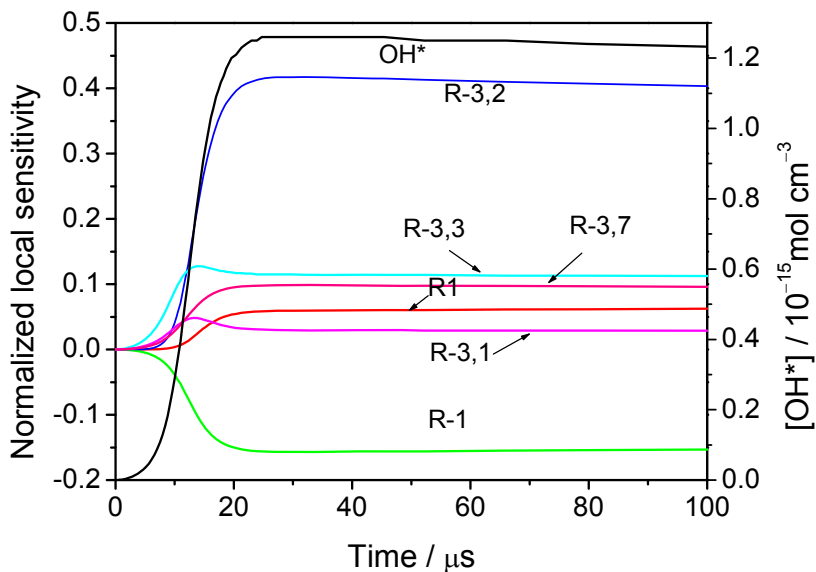


Figure 4: Sensitivity analysis of the OH* formation and destruction at 3000 K showing the dominance of the thermal excitation through reaction (R-3).

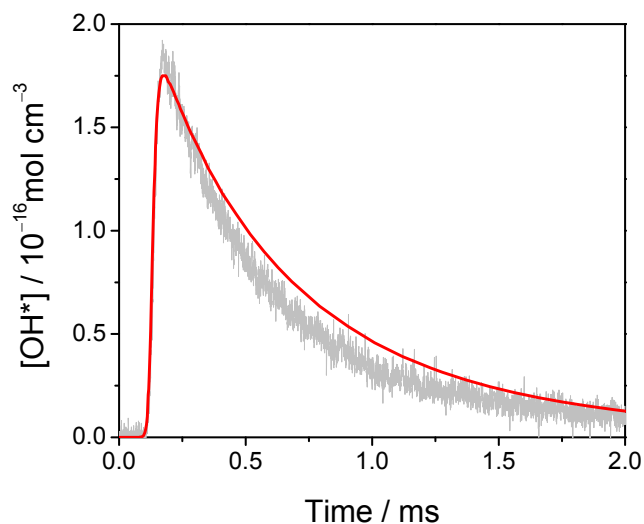


Figure 5: Comparison of the temporal variation of the OH* chemiluminescence I_{OH^*} and the simulated OH* concentration. The experimental absolute concentration is obtained by calibration factor of $2.62 \times 10^{-18} \text{ cm}^3 \text{ mol}^{-1} \text{ mV}^{-1}$ derived from this comparison. The composition of the mixture is 1.0% H₂, 1.0% O₂ diluted in Ar. $T_5 = 1592 \text{ K}$ and $p_5 = 1.27 \text{ bar}$. The simulation is performed with

the rate of reaction (R1) suggested in the present work. The absolute concentration obtained is within available limit of calibration factor uncertainty of $\pm 20\%$.

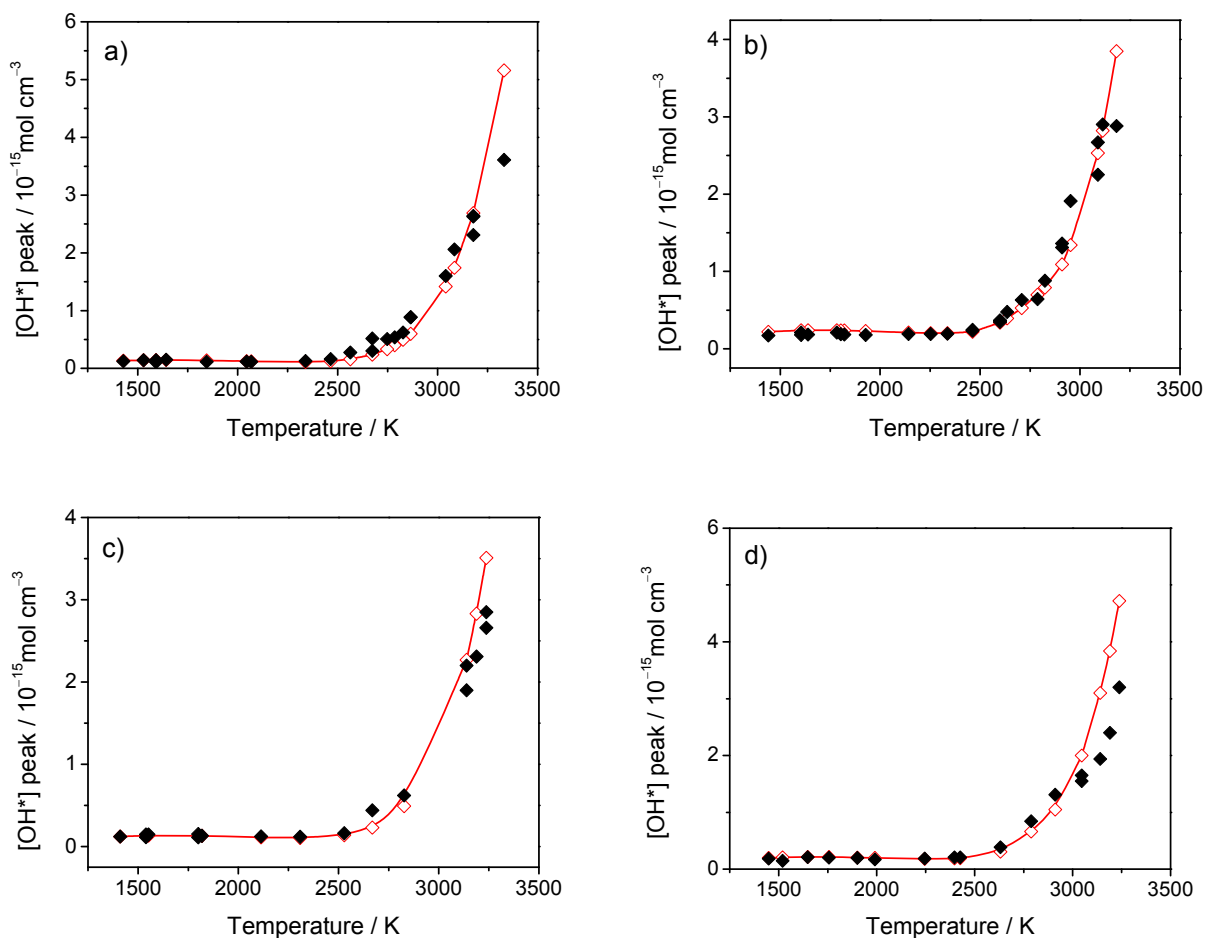


Figure 6: Measured and simulated peak OH* concentration at different temperatures for (a) mixture A, (b) mixture B, (c) mixture C, (d) mixture D. Closed symbols represent experimental data. Open symbols with line represent the simulations at corresponding experimental points with the rate coefficient k_1 of reaction (R1) from the present work. For the chemical compositions, see Table 1.

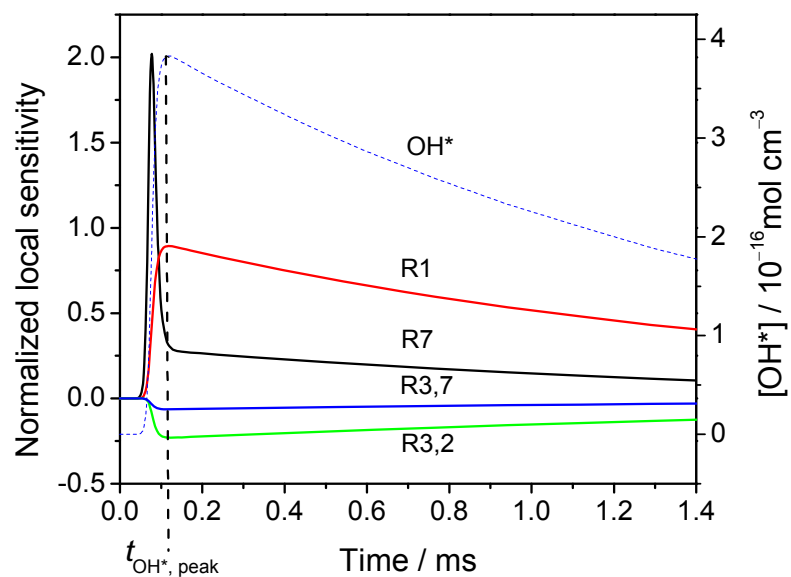


Figure 7: Local sensitivity analysis with respect to OH* over reaction time. Sensitivity coefficients are given as change in OH* concentration due to change in the rate coefficients of the respective reactions. The calculation is done for mixture A at 1900 K and 1 bar. Only the main quenching reactions are shown for clarity.

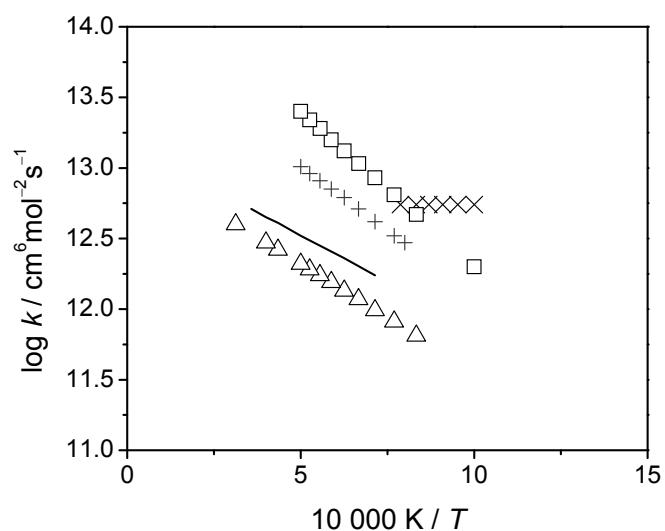


Figure 8: Arrhenius plot for the reaction $\text{H} + \text{O} + \text{M}$ forming OH^* (R1). Symbols: + Koike et al. [4]; Δ Hidaka et al. [3]; \times Smith et al. [1]; \square Hall et al. [5]; — present work.

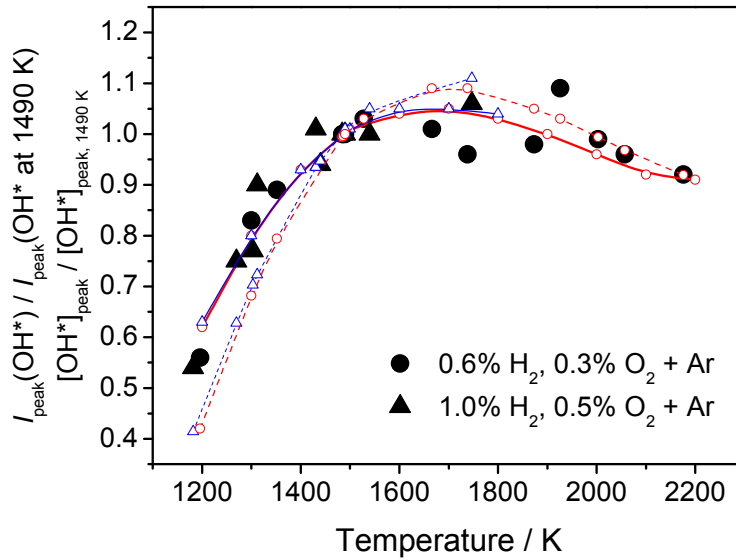


Figure 9: Peak value of OH* emission $I_{\text{peak}}(\text{OH}^*)$ (experiment from [5]) and simulated concentration $[\text{OH}^*]_{\text{peak}}$ at given temperatures normalized to the corresponding value at 1490 K for stoichiometric H₂/O₂/Ar mixtures at 0.97 bar. Closed symbols: Experiments from Hall et al. [5]. Open symbols with solid lines: Simulation with k_1 derived in the present work. Open Symbols with dashed lines are simulations with GRI-mech 3.0 [36] as base mechanism.

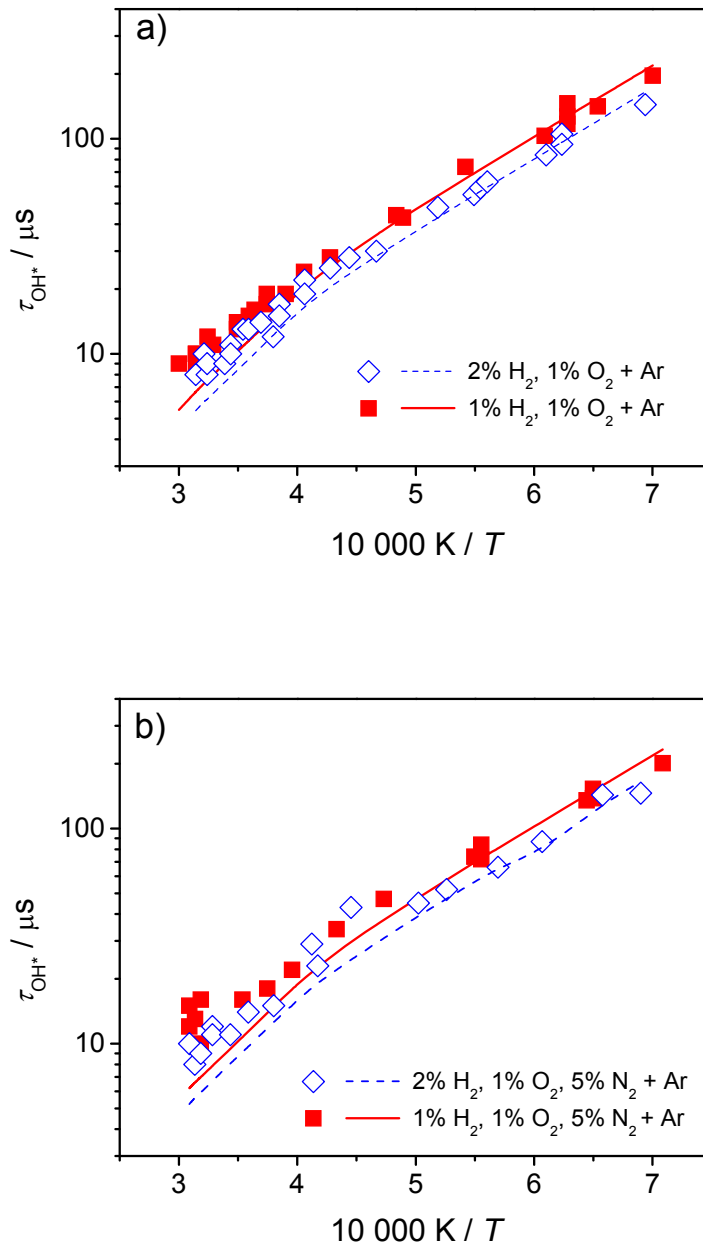


Figure 10: Ignition delay time (τ) with respect to $[\text{OH}^*]$ for stoichiometric and lean H_2/O_2 mixtures with (a) Ar dilution and (b) Ar + N_2 dilution. Symbols: Shock-tube experiments from the present work, Lines: Simulations for the experimental conditions.

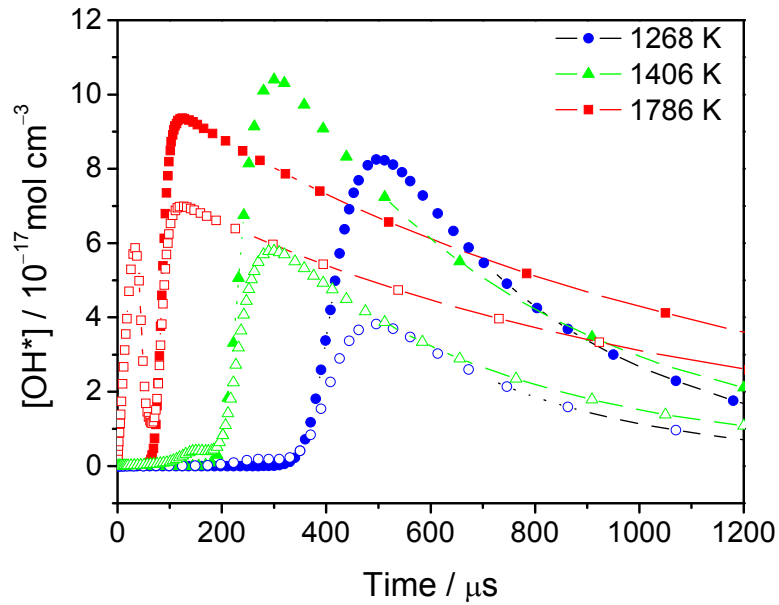


Figure 11: Comparison of simulated OH* concentration profiles for homogeneous conditions obtained by incorporating reaction (R1), with (open symbols) and without (closed symbols with line) reaction (R5) at different temperatures. Mixture composition is 1.0% H₂ and 1.0% O₂ diluted in Ar at 1.2 bar.

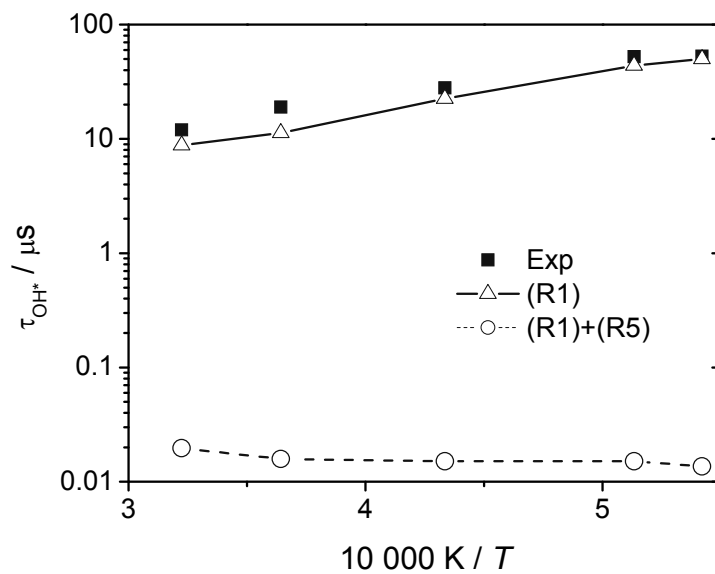


Figure 12: Comparison of measured and simulated ignition delay times in temperature range of 1800–3100 K. The simulated results are related to the steepest gradient in OH* formation from

reaction (R1) and reaction (R1 + R5) in a mixture of % H₂, 1% O₂ in Ar.

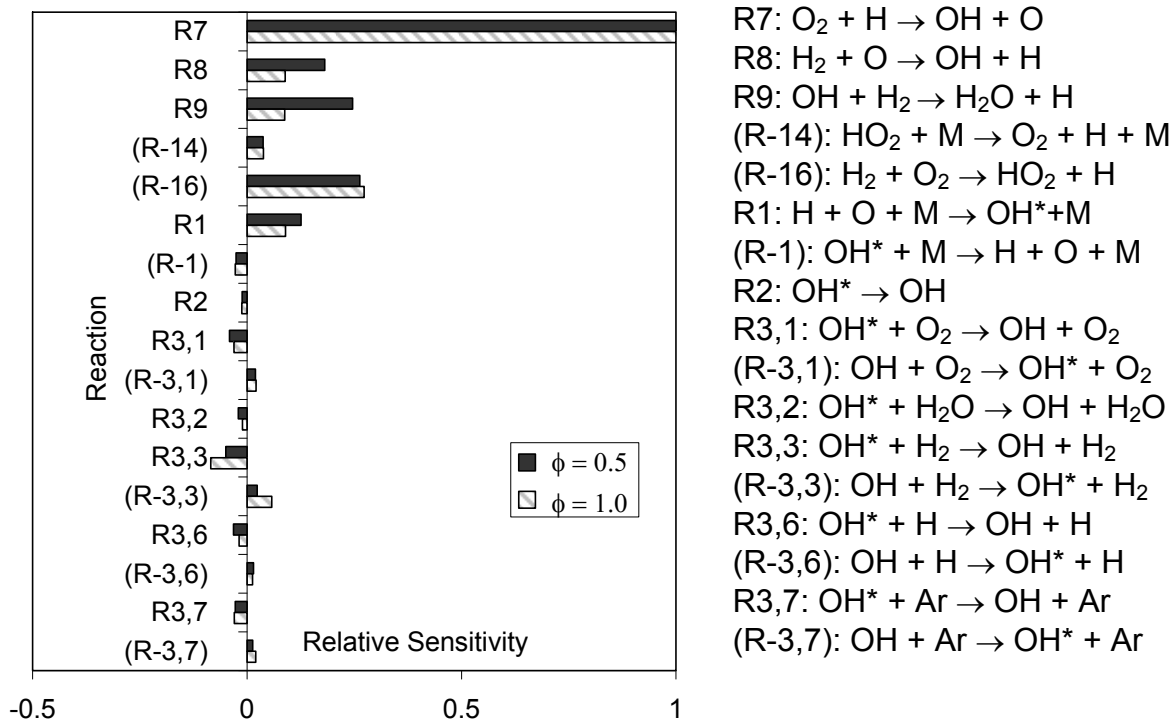


Figure 13: Integral sensitivity analysis with respect to OH* for the induction phase $t \leq 29 \mu s$ (for lean), $t \leq 30 \mu s$ (for stoichiometric) H₂/O₂ mixture with 98% Ar dilution at temperature of 2300 K and pressure of 1 bar under homogeneous conditions.

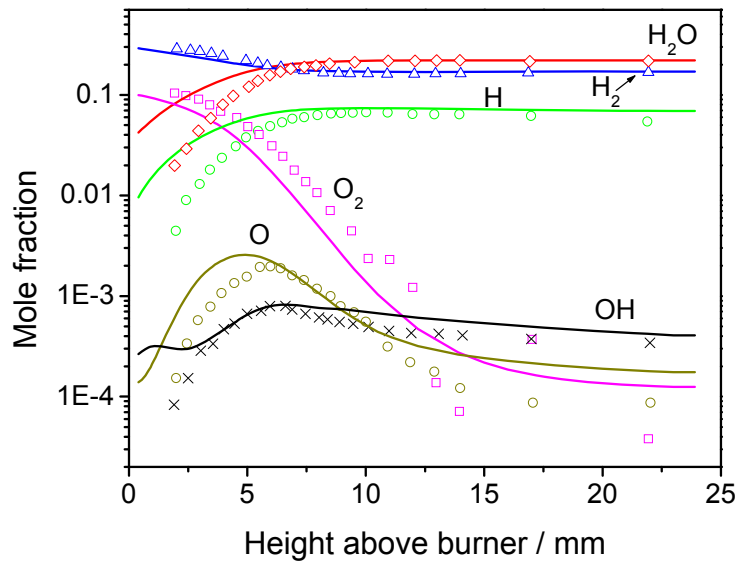


Figure 14: Comparison of absolute concentrations for major radicals and stable species in a rich $\text{H}_2/\text{O}_2/\text{Ar}$ laminar premixed flame at 0.05 bar. Symbols: Experiments [27]; Lines: Simulation.

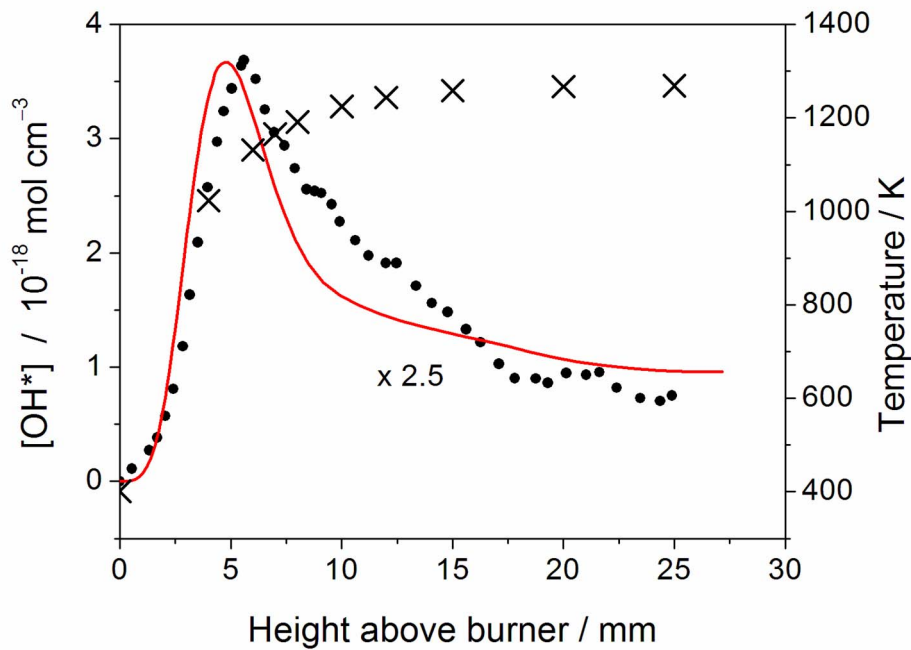


Figure 15: Absolute OH^* concentration profiles as a function of height above burner obtained for a rich ($\phi = 1.54$), low-pressure (0.05 bar), laminar, premixed H_2/air flame. \times Temperature, \bullet $[\text{OH}^*]$ from experiment [1], Line: $[\text{OH}^*]$ from simulation with k_1 from present work, result scaled by a factor

of 2.5.

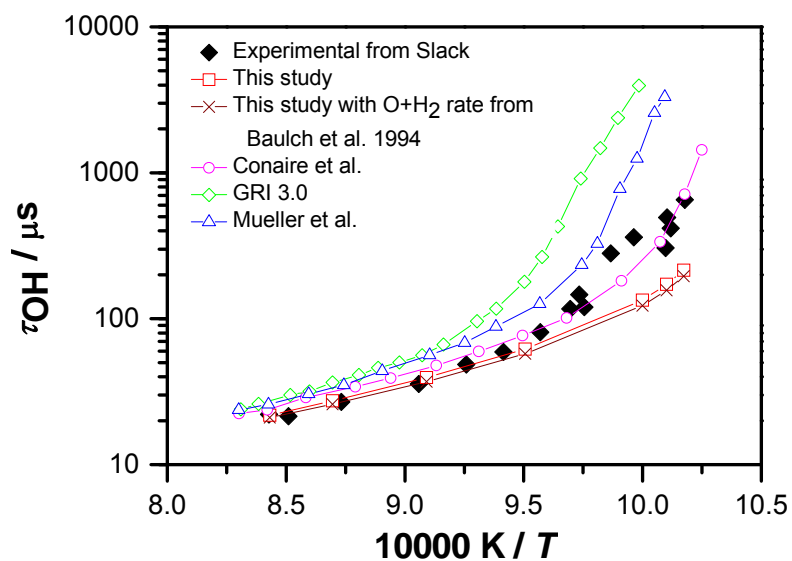


Figure 16: Ignition delay time at 2 bar for stoichiometric H₂/air mixtures. Symbols: experiment from Slack [38]. Open symbols with line: simulations with different literature mechanisms that are shown in fig. 8 of Conaire et al. [31].

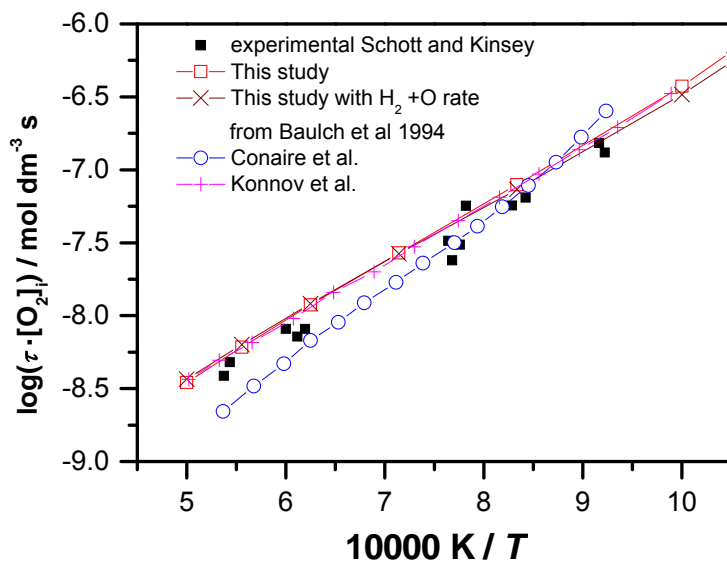


Figure 17: Ignition delay time of 1% H₂, 2% O₂, and 97% Ar mixture at 1 bar. Symbols: Experiment

from Schott and Kinsey [40], Open symbols with line: Simulations with different mechanisms from literature that are presented in fig. 5 of Conaire et al. [31].

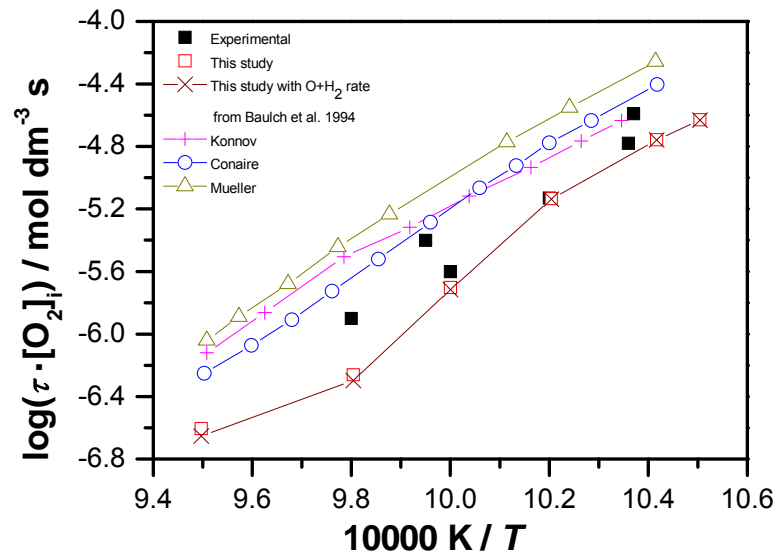


Figure 18: Ignition delay time for 8% H₂, 2% O₂, and 90% Ar at 5 bar measured by Skinner and Ringrose [39]. Symbols: Experiment, Open symbols with line: Simulations with different literature mechanisms that are shown in fig. 4 of Conaire et al. [31].

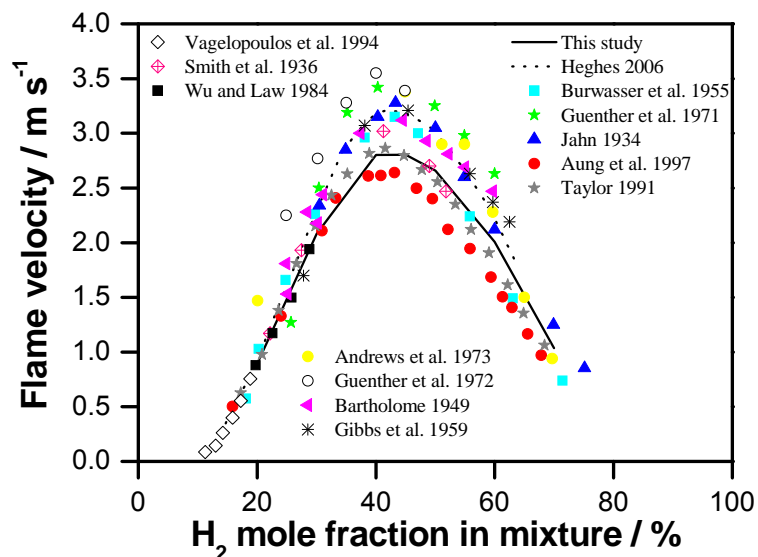


Figure 19: Measured laminar flame velocities of H₂/air mixtures as a function of H₂ mole fraction at 1 bar and 298 K initial temperature. The measurements of flame velocities that are not corrected for stretch effects correspond to the experiments reported in Warnatz [47]. The experiments from Aung et al. [43], Taylor [44], Vagelopoulos et al. [45] and Wu and Law [46] presented here are corrected for flame stretch effects.